recombination in WRN-deficient, telomere dysfunctional cells promotes escape from senescence and engagement of the ALT pathway. *Genes Dev.* **19**, 2560–2570
53. Zeng, S., Xiang, T., Pandita, T.K., Gonzalez-Suarez, I., Gonzalo, S., Harris, C.C., and Yang, Q. (2009) Telomere recombination requires the MUS81 endonuclease. *Nat. Cell Biol.* **11**, 616–623
54. Tarsounas, M., Muñoz, P., Claas, A., Smiraldo, P.G., Pittman, D.L., Blasco, M.A., and West, S.C. (2004) Telomere maintenance requires the RAD51D recombination/repair protein. *Cell* **117**, 337–347
55. Saharia, A. and Stewart, S.A. (2009) FEN1 contributes to telomere stability in ALT-positive tumor cells. *Oncogene* **28**, 1162–1167
56. Grudic, A., Jul-Larsen, A., Haring, S.J., Wold, M.S., Lønning, P.E., Bjerkvig, R., and Bøe, S.O. (2007) Replication protein A prevents accumulation of single-stranded telomeric DNA in cells that use alternative lengthening of telomeres. *Nucleic Acids Res.* **35**, 7267–7278
57. Fan, Q., Zhang, F., Barrett, B., Ren, K., and Andreassen, P.R. (2009) A role for monoubiquitinated FANCD2 at telomeres in ALT cells. *Nucleic Acids Res.* **37**, 1740–1754
58. Jiang, W.Q., Zhong, Z.H., Nguyen, A., Henson, J.D., Toouli, C.D., Braithwaite, A.W., and Reddel, R.R. (2009) Induction of alternative lengthening of telomeres-associated PML bodies by p53/p21 requires HP1 proteins. *J. Cell Biol* **185**, 797–810
59. De'jardin, J. and Kingston, R.E. (2009) Purification of proteins associated with specific genomic Loci. *Cell* **136**, 175–186
60. Perrem, K., Bryan, T.M., Englezou, A., Hackl, T., Moy, E.L., and Reddel, R.R. (1999) Repression of an alternative mechanism for lengthening of telomeres in somatic cell hybrids. *Oncogene* **18**, 3383–3390
61. Lundblad, V. and Blackburn, E.H. (1993) An alternative pathway for yeast telomere maintenance rescues est1-senescence. *Cell* **73**, 347–360
62. Teng, S.C. and Zakian, V.A. (1999) Telomere-telomere recombination is an efficient bypass pathway for telomere maintenance in Saccharomyces cerevisiae. *Mol. Cell Biol.* **19**, 8083–8093
63. Lin, C.Y., Chang, H.H., Wu, K.J., Tseng, S.F., Lin, C.C., Lin, C.P., and Teng, S.C. (2005) Extrachromosomal telomeric circles contribute to Rad52-, Rad50-, and polymerase delta-mediated telomere-telomere recombination in Saccharomyces cerevisiae. *Eukaryot. Cell* **4**, 327–336
64. Natarajan, S., Groff-Vindman, C., and McEachern, M.J. (2003) Factors influencing the recombinational expansion and spread of telomeric tandem arrays in Kluyveromyces lactis. *Eukaryot Cell* **2**, 1115–1127
65. Natarajan, S. and McEachern, M.J. (2002) Recombinational telomere elongation promoted by DNA circles. *Mol. Cell Biol.* **22**, 4512–4521
66. Niida, H., Shinkai, Y., Hande, M.P., Matsumoto, T., Takehara, S., Tachibana, M., Oshimura, M., Lansdorp, P.M., and Furuichi, Y. (2000) Telomere maintenance in telomerase-deficient mouse embryonic stem cells: characterization of an amplified telomeric DNA. *Mol. Cell Biol.* **20**, 4115–4127
67. Chang, S., Khoo, C.M., Naylor, M.L., Maser, R.S., and DePinho, R.A. (2003) Telomere-based crisis: functional differences between telomerase activation and ALT in tumor progression. *Genes Dev.* **17**, 88–100
68. Gonzalo, S., Jaco, I., Fraga, M.F., Chen, T., Li, E., Esteller, M., and Blasco, M.A. (2006) DNA methyltransferases control telomere length and telomere recombination in mammalian cells. *Nat. Cell Biol.* **8**, 416–424
69. Tilman, G., Loriot, A., Van Beneden, A., Arnoult, N., Londoño-Vallejo, J.A., De Smet, C., and Decottignies, A. (2009) Subtelomeric DNA hypomethylation is not required for telomeric sister chromatid exchanges in ALT cells. *Oncogene* **28**, 1682–1693
70. Yankiwski, V., Marciniak, R.A., Guarente, L., and Neff, N.F. (2000) Nuclear structure in normal and Bloom syndrome cells. *Proc. Natl Acad. Sci. USA* **97**, 5214–5219
71. Wu, G., Jiang, X., Lee, W.H., and Chen, P.L. (2003) Assembly of functional ALT-associated promyelocytic leukemia bodies requires Nijmegen Breakage Syndrome 1. *Cancer Res.* **63**, 2589–2595
72. Zhu, X.D., Niedernhofer, L., Kuster, B., Mann, M., Hoeijmakers, J.H., and de Lange, T. (2003) ERCC1/XPF removes the 3′ overhang from uncapped telomeres and represses formation of telomeric DNA-containing double minute chromosomes. *Mol. Cell* **12**, 1489–1498
73. Moran-Jones, K., Wayman, L., Kennedy, D.D., Reddel, R.R., Sara, S., Snee, M.J., and Smith, R. (2005) hnRNP A2, a potential ssDNA/RNA molecular adapter at the telomere. *Nucleic Acids Res.* **33**, 486–496
74. Zhu, X.D., Kuster, B., Mann, M., Petrini, J.H., and de Lange, T. (2000) Cell-cycle-regulated association of RAD50/MRE11/NBS1 with TRF2 and human telomeres. *Nat. Genet.* **25**, 347–352
75. Dantzer, F., Giraud-Panis, M.J., Jaco, I., Amé, J.C., Schultz, I., Blasco, M., Koering, C.E., Gilson, E., Ménissier-de Murcia, J., de Murcia, G., and Schreiber, V. (2004) Functional interaction between poly(ADP-Ribose) polymerase 2 (PARP-2) and TRF2: PARP activity negatively regulates TRF2. *Mol. Cell Biol.* **24**, 1595–1607
76. Silverman, J., Takai, H., Buonomo, S.B., Eisenhaber, F., and de Lange, T. (2004) Human Rif1, ortholog of a yeast telomeric protein, is regulated by ATM and 53BP1 and functions in the S-phase checkpoint. *Genes Dev.* **18**, 2108–2119
77. Miyake, Y., Nakamura, M., Nabetani, A., Shimamura, S., Tamura, M., Yonehara, S., Saito, M., and Ishikawa, F. (2009) RPA-like mammalian Ctc1-Stn1-Ten1 complex binds to single-stranded DNA and protects telomeres independently of the Pot1 pathway. *Mol. Cell* **36**, 193–206
78. Johnson, F.B., Marciniak, R.A., McVey, M., Stewart, S.A., Hahn, W.C., and Guarente, L. (2001) The Saccharomyces cerevisiae WRN homolog Sgs1p participates in telomere maintenance in cells lacking telomerase. *EMBO J.* **20**, 905–913
79. Opresko, P.L., Otterlei, M., Graakjaer, J., Bruheim, P., Dawut, L., Kølvraa, S., May, A., Seidman, M.M., and Bohr, V.A. (2004) The Werner syndrome helicase and exonuclease cooperate to resolve telomeric D loops in a manner regulated by TRF1 and TRF2. *Mol. Cell* **14**, 763–774

Jpn J Radiol (2009) 27:115–122
DOI 10.1007/s11604-008-0307-y

ORIGINAL ARTICLE

Volume of pulmonary lobes and segments in chronic obstructive pulmonary diseases calculated using newly developed three-dimensional software

Tadahisa Daimon · Kiminori Fujimoto · Keisuke Tanaka
Junya Yamamoto · Kanako Nishimura · Yuko Tanaka
Masahiro Yanagawa · Hiromitsu Sumikawa
Atsuo Inoue · Osamu Honda · Noriyuki Tomiyama
Hironobu Nakamura · Yukihiko Sugiyama
Takeshi Johkoh

Received: October 17, 2008 / Accepted: November 25, 2008

Abstract
Purpose. The aim of this study was to measure the volume of each pulmonary segment by volumetric computed tomography (CT) data using a newly developed three-dimensional software application and to identify the differences between those with chronic obstructive pulmonary disease (COPD) and controls.
Materials and methods. CT scans of 11 COPD patients and 16 controls were included. The volume of each pulmonary segment was measured by each of two operators to evaluate the reproducibility of the software. This measured volume was then divided by the total lung volume to revise individual variations.
Results. Volumes of the right (rt) S2, rt S5, left (lt) S1 + S2, lt S3, and lt S5 were significantly larger in COPD patients than in controls ($P < 0.05$). Regarding the ratio of the volume of each pulmonary segment per total lung volume, the areas of rt S2 and lt S1 + S2 were significantly larger in COPD patients than in controls ($P < 0.05$), whereas lt S10 was significantly smaller in COPD patients than in controls ($P < 0.05$).
Conclusion. We measured the volume of each pulmonary segment based on volumetric CT data using this software. In addition, we demonstrated that the upper lung volume of COPD subjects was larger than that of controls, whereas the lower lung volumes were almost the same.

Key words Chronic obstructive pulmonary disease · Computed tomography · Pulmonary segment

T. Daimon · Y. Tanaka · M. Yanagawa · H. Sumikawa · A. Inoue · O. Honda · N. Tomiyama · H. Nakamura
Department of Radiology, Osaka University Graduate School of Medicine, Suita, Japan

K. Tanaka · J. Yamamoto · K. Nishimura
Department of Medical Physics, Osaka University Graduate School of Medicine, Suita, Japan

T. Daimon (✉) · Y. Sugiyama
Department of Medicine, Division of Pulmonary Medicine, Jichi Medical University, 3311-1 Yakushiji, Shimotsuke, Tochigi 329-0498, Japan
Tel. +81-285-58-7350; Fax +81-285-44-3586
e-mail: tada0605@jichi.ac.jp

K. Fujimoto
Department of Radiology, Kurume University School of Medicine, Kurume, Japan

T. Johkoh
Department of Radiology, Kinki Central Hospital, Itami, Japan

Introduction

Chronic obstructive pulmonary disease (COPD) is a disease state characterized by airflow limitation that is not fully reversible.[1] The chronic airflow limitation in COPD is caused by a mixture of small airway disease (obstructive bronchiolitis) and parenchymal destruction (emphysema), the relative contributions of which vary from person to person. Chronic inflammation causes remodeling and narrowing of the small airways. Destruction of the lung parenchyma, also by inflammatory processes, leads to the loss of alveolar attachments to the small airways. A diagnosis of COPD should be confirmed by an objective measure of airflow limitation.[1]

Airflow limitation is measured by spirometry, as this is the most widely available, reproducible, and standardized test of lung function. Forced expiratory volume in 1 s (FEV_1)/forced vital capacity (FVC) < 70% and a postbronchodilator FEV_1 < 80% predicted confirms the presence of airflow limitation that is not fully reversible. The four-stage classification based on postbronchodilator FEV_1 of COPD severity used throughout the Global Initiative for Chronic Obstructive Lung Disease (GOLD) guideline[1] provides an educational tool and a general indication of the approach to management.

Computed tomography (CT) in COPD is used to evaluate emphysema by detecting low attenuation areas (LAAs); thus, the role of CT has been well established.[2–4] Recent progress in CT technology has made it possible to detect and quantify faint airway abnormalities.[5–7] Longitudinally increasing changes in LAA in smoking-induced lung disease have been observed, predominantly in the upper lung field.[8] However, there are no reports of having evaluated pulmonary segmentation volumes using CT in any pulmonary disease, including COPD.

The aim of this study was to measure the volume of each pulmonary segment based on volumetric CT data using a newly developed software application and to identify the differences between those with COPD and controls.

Materials and methods

Subjects

Between November 2005 and May 2006, a series of 11 consecutive patients with COPD and 16 controls who underwent pulmonary function tests and CT at our institutions were entered into the study. The patients with COPD included 10 men and 1 woman aged 68 ± 5 years (mean ± SD) (range 59–77 years). The subjects were either current smokers ($n = 8$) or former smokers ($n = 3$). The controls included 6 men and 10 women aged 54 ± 15 years (mean ± SD) (range 19–72 years). The subjects were either current smokers ($n = 3$) or had never smoked ($n = 16$). The institutional review board gave full approval and waived informed consent for our retrospective study.

A diagnosis of COPD was made based on the Global Initiative for Chronic Obstructive Lung Disease (GOLD) guideline.[1] Subjects who had an allergic diathesis, an episodic wheeze, or a history of bronchial asthma were excluded from this study. Patients with COPD in various clinical stages according to the GOLD criteria (stage I, $n = 6$; stage II, $n = 2$; stage III, $n = 1$; stage IV, $n = 2$) were enrolled. The subjects' characteristics are shown in Table 1.

Pulmonary function tests

Pulmonary function tests were performed within a month before CT or after CT. The spirometric measurements were made on a pneumotachograph (Chestac-33; Chest, Tokyo, Japan). The results of the pulmonary function tests met the requirements of the Japanese Respiratory Society guidelines,[9] which are similar to those of the American Thoracic Society (ATS). FEV_1 and FVC were measured before and 15 min after inhalation of a short-acting β_2-agonist (20 μg procaterol hydrochloride). The vital capacity (VC) and FEV_1 were expressed as a percentage of predicted values according to the prediction

Table 1. Characteristics of COPD patients and controls

Characteristic	Patients with COPD (mean)	Controls (mean)
Age (years)	68 ± 5	54 ± 15*
Height (cm)	166 ± 7	158 ± 9
Weight (kg)	58 ± 7	60 ± 13
Smoking index (pack-years)	98.0 ± 144.7	21.7 ± 1.4*
VC (l)	3.42 ± 0.95	3.15 ± 1.07
VC (% predicted)	103.0 ± 24.8	111.6 ± 18.7
FEV_1 (l)	1.89 ± 0.93	2.42 ± 0.85
FEV_1/FVC (%)	53.6 ± 19.4	77.7 ± 6.37*
FEV_1 (% predicted)	75.5 ± 35.6	107.1 ± 18.1*
RV/TLC (%)	31.2 ± 10.4	26.7 ± 7.82
DLco/VA (ml/min/mmHg/l)	4.73 ± 1.27	4.85 ± 0.87

COPD, chronic obstructive pulmonary disease; VC, vital capacity; FEV_1, forced expiratory volume in 1 s; FVC, forced vital capacity; RV, residual volume; TLC, total lung capacity; DLco, carbon monoxide diffusion in the lung; VA, alveolar ventilation
Data are shown as means ± SD
FVC and FEV_1 tests were performed after the inhalation of a short-acting β_2-agonist
* $P < 0.05$ vs controls

equations of the Japanese Respiratory Society.[9] Lung volumes, total lung capacity (TLC), functional residual capacity (FRC), and residual volume (RV) were measured by the helium closed-circuit method. Carbon monoxide diffusing capacity (DLCO) and DLCO divided by alveolar volume (VA) were measured with the single-breath method according to the pulmonary function test guidelines of the Japanese Respiratory Society.[9] The percent predicted values for DLCO and DLCO/VA were determined using the method of Nishida et al.[10]

Computed tomography techniques

All CT scans were performed at the end of inspiration with the patient in the supine position; no intravenous contrast material was used. All CT images were acquired on a 16-detector row CT scanner (LightSpeed Ultra system; GE Healthcare, Milwaukee, WI, USA). Scanning parameters were 120 kVp and 200 mA. Scanning was performed using a pitch of 1.375:1.0, a 0.6-s scanning time per rotation, a table speed of 13.75 mm/rotation, and a detector configuration of 0.625 × 16 mm. The CT data for each phase were retrospectively reconstructed using a standard algorithm at a reconstruction interval of 0.625 mm with 0.625 mm section thickness (window level –600 HU; window width 1500 HU). The imaging data were transferred automatically to a workstation (Virtual Place version 2.03; Aze, Tokyo, Japan) in a 512 × 512 pixel format online.

Outline of software for calculation of volume of pulmonary segments

For this study, we developed new software for measuring the volumes of pulmonary segments. The software was produced as a plug-in of Virtual Place version 2.03 (Aze) with Visual Studio .NET 2003 C++ (Microsoft, Edmond, WA, USA). The lung three-dimensional (3D) images from CT were obtained by threshold processing (Fig. 1). At first, both lungs were separated into two or three lobes along the lung interlobar fissures. We used the sheet filter, a 3D line enhancement filter, that was developed with the aim of discriminating line structures from other structures and recovering line structures of various widths.[11] Furthermore, we improved the sheet filter to emphasize only the fissures (Fig. 2). Emphasized fissures (Fig. 2) had some holes and areas lacking in each extracted fissure. Therefore, emphasized fissures were interpolated by the thin plate spline method. The thin plate spline method, a general algorithm for interpolation in multidimensional space, is a conventional tool for surface interpolation over scattered data.[12,13] The interpolated fissures were then used as boundary surfaces between lobes (Figs. 3, 4).

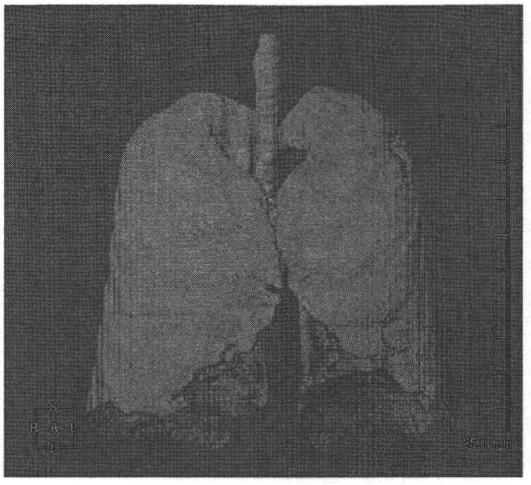

Fig. 1. Lung mask image. Three-dimensional (3D) computed tomography (CT) images of the lung were obtained by threshold processing

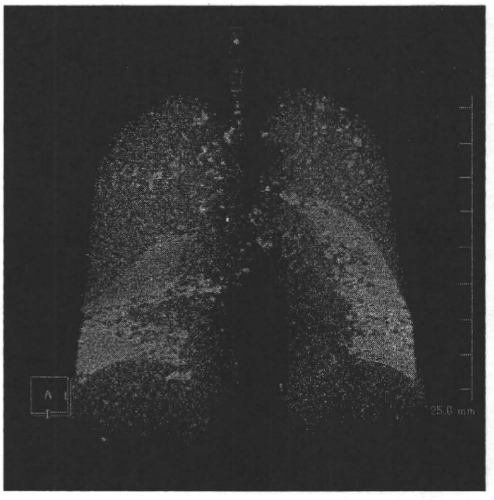

Fig. 2. Emphasized image by the sheet filter method. Note that the emphasized image had many areas of noise

Borders of segments were anatomically defined as the virtual surfaces where subsegmental veins run. Thus, to determine the borders, we first used previously developed vessel-tracking software. The details of vessel-tracking software show a user how to set the initial tracking point and orientation, and the software then automatically tracks center lines and determines branch and terminal points as well as new points and orientations at the detected branch points for restarting the tracking. The operator sets the initial tracking point of the subsegmental veins on a CT image (Fig. 5) and saves

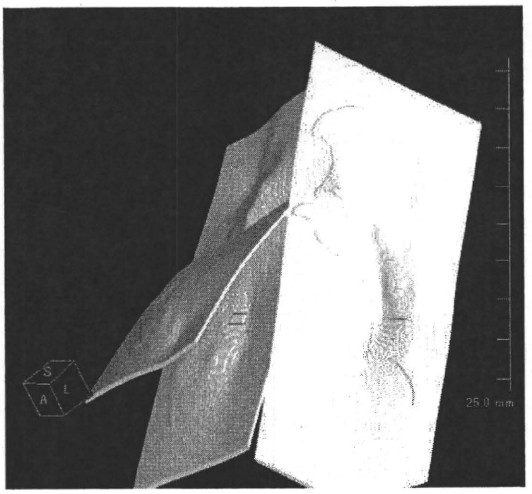

Fig. 3. Interpolated fissures. Processed image with the thin plate spline method from an extracted fissure image

Fig. 5. Tracking root (*gray line*) of a subsegmental vein on a CT image

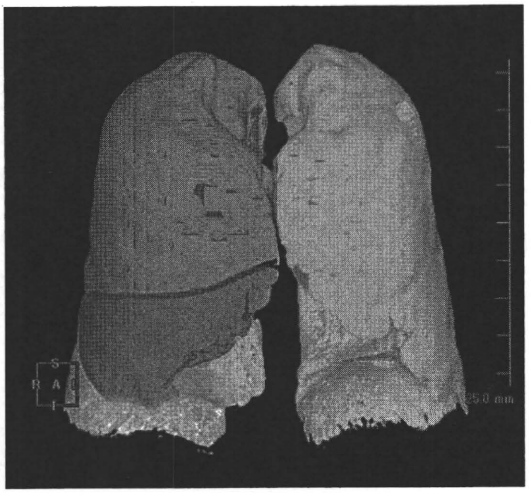

Fig. 4. Lung lobe image at the 3D workstation. The lung mask image (Fig. 1) was divided into lung lobes using interpolated fissures. The right lung was divided into three lobes and the left one into two lobes

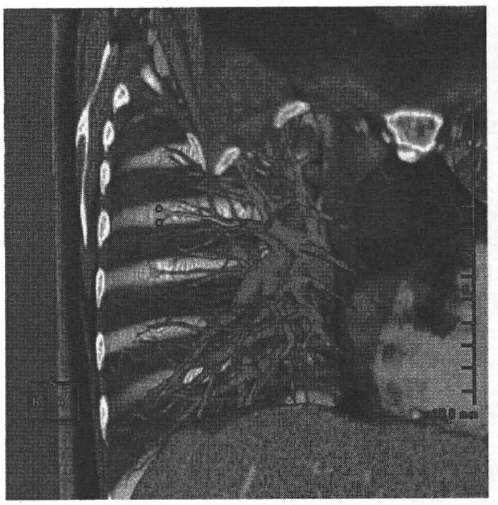

Fig. 6. Image of a tracing purpose subsegmental vein. The tracking root of a subsegmental vein is shown in XML format

the tracking root of each subsegmental vein in XML format (Fig. 6). The virtual surfaces of segments are formed from the saved tracking roots of the subsegmental veins and are interpolated using the thin plate spline method. Using these borders, the lung lobes are divided into pulmonary segments on a 3D image (Fig. 7). Voxels of each pulmonary segment can then be calculated automatically and described as the volume of the pulmonary segment. Furthermore, with the multiplanar reconstruction imaging (MPR) view, the user can view the image of the colored pulmonary segment (Fig. 8).

Analysis of pulmonary segmentation volume

The CT scans were randomized, and then each volume of pulmonary segment was measured by each of two operators (developer and chest radiologist) independently to evaluate the reproducibility of this software. The operators were unaware of any clinical findings other than the patient's age and sex. Data for each volume of the pulmonary segment measured by the software was analyzed for statistical differences between the COPD group and the controls. Furthermore, each volume of the pulmonary segment was divided by the total of the two lung volumes to revise individual variations.

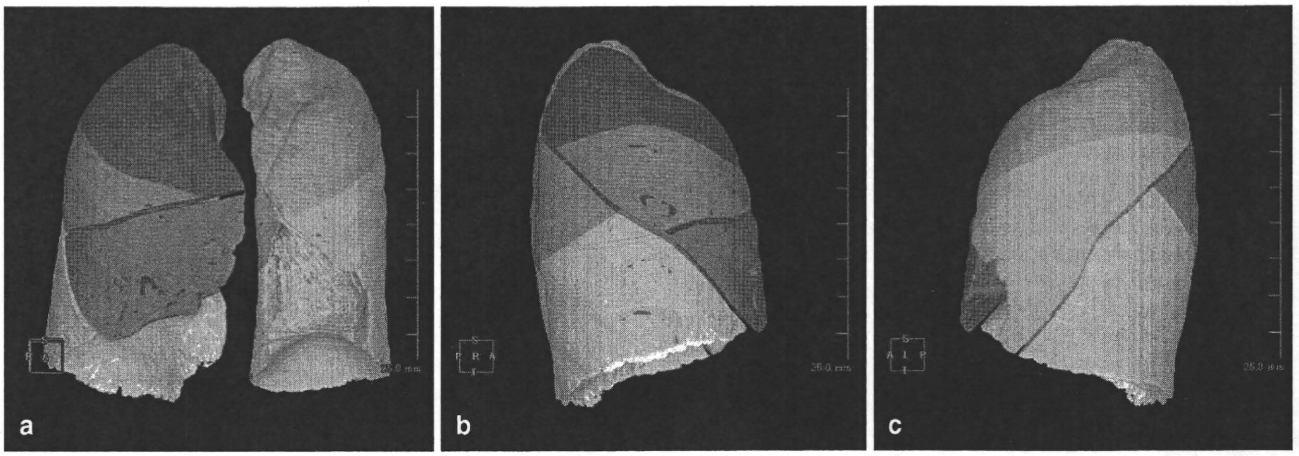

Fig. 7. Pulmonary segment images at a 3D workstation. The lung lobe image (Fig. 4) was divided into pulmonary segments using traced subsegmental vein data. **a** Front view. **b** Right view. **c** Left view

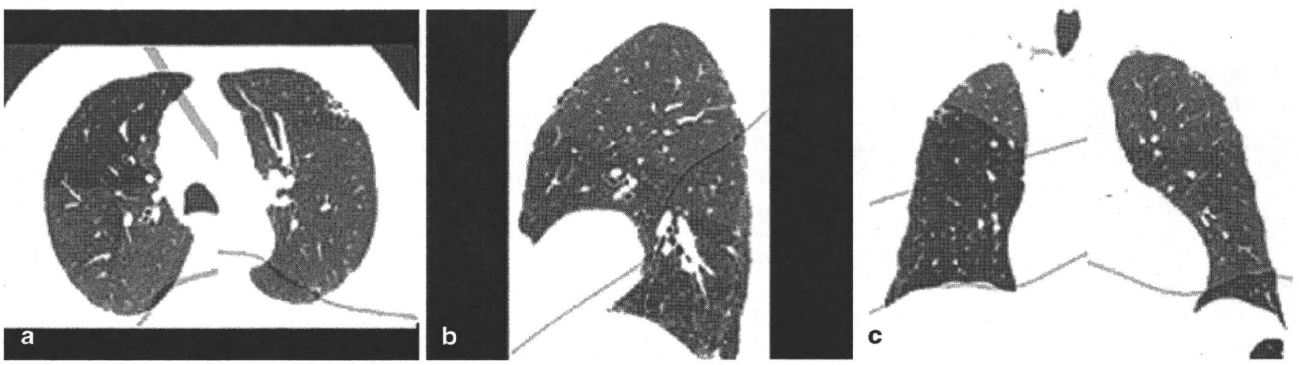

Fig. 8. Multiplanar reconstruction (MPR) fusion images of a coloring pulmonary segment. **a** Axial view. **b** Sagittal view. **c** Coronal view

Statistical analysis

The reproducibility of this software was analyzed with a Bland-Altman plot, using Excel (Microsoft) software. Furthermore, correlation of two data points was analyzed using Pearson's correlation coefficient. The data of the developer are shown as the mean ± SD. Differences between two variables were assessed using the Mann-Whitney U-test. All statistical analyses were performed with statistical software (SPSS, version 12.0J; SPSS, Tokyo, Japan).

Results

Reproducibility of software

The results of the Bland-Altman plot between the two operators are shown in Fig. 9. The x-axis of this graph displays the mean of two pulmonary segmentation volumes. The y-axis displays the difference between the two pulmonary segmentation volumes. The mean difference between the two operators was 0 cm^3 (Fig. 9). The limits of reproducibility were –83.33 and 83.33 cm^3 (mean ± 2 SD) (Fig. 9). There was statistically good correlation between the data ($P < 0.001$, $r = 0.948$).

Pulmonary segmentation volume

The pulmonary segment volumes in patients with COPD and the controls are shown in Table 2. In the upper lobe of the right lung, the volume of the posterior segment, S2, in patients with COPD was significantly larger than in the controls ($P < 0.05$) (COPD vs. control subjects 235 ± 92 vs. 122 ± 50 cm^3). In the middle lobe, the volume of the medial segment, S5, in patients with COPD was significantly larger than that in the controls ($P < 0.05$) (COPD vs. control subjects: 352 ± 116 vs. 231 ± 94 cm^3). In the lower lobe of the right lung, the volumes of all segments in patients with COPD did not differ from

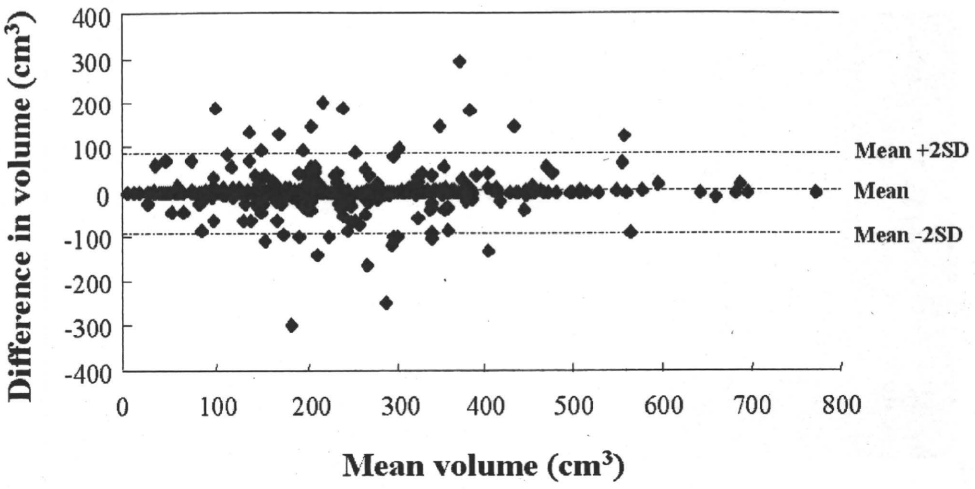

Fig. 9. Bland-Altman plot of the pulmonary segmentation volume. This graph was plotted to compare two results of the calculated pulmonary segmentation volume. Horizontal axis indicates the mean of two results. Vertical axis indicates the difference between two results. *Dashed line*, mean difference in volume; *dotted-dashed line*, mean difference ± 2 SD

Table 2. Pulmonary segmentation volume of COPD patients and controls

Segmentation	Patients with COPD (n = 11)	Controls (n = 16)	P
Right lung	(cm^3)	(cm^3)	
Upper lobe			
S1	466 ± 191 (9.6% ± 3.2%)	334 ± 93 (9.3% ± 2.3%)	0.076 (0.980)
S2	235 ± 92 (4.9% ± 1.5%)	122 ± 50 (3.5% ± 1.8%)	0.002* (0.032*)
S3	357 ± 130 (7.7% ± 2.7%)	269 ± 98 (7.5% ± 2.7%)	0.114 (0.786)
Middle lobe			
S4	110 ± 59 (2.3% ± 1.1%)	102 ± 46 (2.9% ± 1.7%)	0.675 (0.444)
S5	352 ± 116 (7.4% ± 1.8%)	231 ± 94 (6.3% ± 2.0%)	0.020* (0.191)
Lower lobe			
S6	235 ± 59 (5.1% ± 1.5%)	234 ± 114 (6.2% ± 2.0%)	0.604 (0.191)
S7	64 ± 43 (1.4% ± 0.9%)	66 ± 43 (1.7% ± 0.9%)	0.980 (0.289)
S8	235 ± 84 (4.9% ± 1.4%)	207 ± 93 (5.5% ± 1.5%)	0.267 (0.416)
S9	188 ± 88 (4.0% ± 1.8%)	179 ± 94 (4.8% ± 1.9%)	0.711 (0.312)
S10	276 ± 103 (5.8% ± 1.5%)	255 ± 102 (6.9% ± 1.7%)	0.604 (0.109)
Left lung			
Upper lobe			
S1+2	451 ± 123 (9.7% ± 2.1%)	300 ± 101 (8.1% ± 1.2%)	0.001* (0.014*)
S3	404 ± 162 (8.3% ± 2.3%)	270 ± 101 (7.5% ± 2.3%)	0.026* (0.361)
S4	208 ± 96 (4.5% ± 2.0%)	143 ± 51 (4.0% ± 1.5%)	0.057 (0.824)
S5	266 ± 113 (5.6% ± 2.1%)	178 ± 88 (4.8% ± 1.8%)	0.028* (0.227)
Lower lobe			
S6	228 ± 62 (4.9% ± 1.4%)	188 ± 77 (5.1% ± 1.5%)	0.191 (0.748)
S8	218 ± 109 (4.6% ± 1.8%)	160 ± 78 (4.2% ± 1.4%)	0.175 (0.604)
S9	259 ± 103 (5.4% ± 1.8%)	238 ± 119 (6.4% ± 2.6%)	0.587 (0.416)
S10	190 ± 87 (3.9% ± 1.4%)	210 ± 129 (5.6% ± 2.4%)	0.941 (0.034*)

Data are shown as means ± SD
Data in parentheses are percentages of the pulmonary segmentation volume divided by the total of both lung volumes
Data in parentheses for the P value are against data divided by the total of both lung volumes
* $P < 0.05$ vs controls

those of the controls. In the upper lobe of the left lung, the volumes of the apicoposterior segment, S1+2, the anterior segment, S3, and the inferior lingular segment, S5, in patients with COPD were significantly larger than in the controls ($P < 0.05$) (S1+2: COPD vs. control subjects 451 ± 123 vs. 300 ± 101 cm^3; S3: COPD vs. control subjects 404 ± 162 cm^3 vs. 270 ± 101 cm^3; S5: COPD vs. control subjects 266 ± 113 cm^3 vs. 178 ± 88 cm^3). In the lower lobe of the left lung, the volumes of all segments in patients with COPD did not differ from those of the controls.

Regarding each volume of pulmonary segment/total lung volume ratio, the areas of the right (rt) S2 and left (lt) S1+2 in COPD patients were significantly larger than those in the controls ($P < 0.05$) (rt S2: COPD vs. control subjects 4.9% ± 1.5% vs. 3.5% ± 1.8%; lt S1+2: COPD

vs. control subjects 9.7% ± 2.1% vs. 8.1% ± 1.2%). The ratio of the lt S10 in COPD patients was significantly smaller than that in the controls ($P < 0.05$) (COPD vs. control subjects 3.9% ± 1.4% vs. 5.6% ± 2.4%).

Discussion

The present study is the first to measure the volume of each pulmonary segment based on CT data and new software and to use this information to identify the differences between COPD patients and controls. We found that the upper lung volume of those with COPD is larger than in controls, although the lower lung volume of COPD patients is almost the same as in controls.

Worldwide, cigarette smoking is the most commonly encountered risk factor for COPD.[1] Pulmonary function tests often show findings of chronic airflow limitation in patients who have emphysema, and these patients are diagnosed as having COPD. In particular, centrilobular emphysema usually results from cigarette smoking and primarily involves the upper lung zones.[14] In this study, the volumes of pulmonary segments rt S2, lt S1+2, and lt S3 in COPD patients were significantly larger than those in the controls (Table 2). Soejima et al.[8] reported that longitudinally increasing changes in LAAs in smoking-induced damaged lungs were predominantly observed in the upper lung field. All of the COPD patients in the present study were either current or former smokers, and the results of this study support these facts. Furthermore, the volumes of pulmonary segments rt S5 and lt S5 in COPD patients were also significantly larger than those in the controls (Table 2). The pulmonary segments rt S5 and lt S5 in patients with COPD might have tendency to inflate compared with those of normal patients, caused by air trapping or emphysematous change itself. The middle lobe and lingular bronchi are easy to compress or obstruct, resulting in the collapse or atelectasis that has been called the middle lobe syndrome. This also might be reflected the phenomenon of decreasing volumes of pulmonary segments rt S5 and lt S5 in controls compared with those of COPD patients.

In general, physiological lung volume has diverse individual variation. In the present study, each pulmonary segmentation volume was divided by the total both-lung volume to revise individual variations. The volumes of pulmonary segments rt S2, rt S5, lt S1+2, lt S3, and lt S5 in COPD patients were significantly larger than those in the controls. However, in the volume of each pulmonary segment/total lung volume ratio, only two areas—rt S2 and lt S1+2—in COPD lungs were significantly greater than in the controls. As the height and weight of patients with COPD did not different from those of the controls, this result has two possible explanations: (1) both the volume of each pulmonary segment and the total lung volume increased; or (2) there was a relatively small number of COPD patients in this study.

Currently, researchers, particularly Japanese investigators, consider COPD to have two clinical phenotypes: an emphysema-dominant phenotype and an airway disease-dominant phenotype.[15] The airway disease-dominant phenotype is more common than the emphysema-dominant phenotype in women and in nonsmokers.[15] Clinical phenotypes of COPD have been classified according to the findings of high-resolution computed tomography (HRCT).[16,17] Comparing the volume of each pulmonary segment in two clinical phenotypes might be useful to elucidate the differences between the clinical phenotypes of COPD. Unfortunately, the number of COPD patients in the present study was insufficient to analyze the differences in clinical phenotypes.

There are some limitations of the present study. First, the software was assessed to have statistically good correlation between the result of the developer and that of the chest radiologist ($P < 0.001$, $r = 0.948$). However, as shown in Fig. 9, there were 32 cases that were outlying the range (y-axis: mean difference ± 2 SD) between the two data sets. This is because we used vessel-tracking software to extract the vessel-running data. Briefly, using vessel-tracking software, we determined the subsegmental vein forming each pulmonary segment ourselves, and thus determination of a false vessel would have resulted in an incorrect pulmonary segment border. Thus, the user must have sufficient knowledge of lung vessel running to determine the correct subsegmental veins. Therefore, we need to develop an algorithm that automatically tracks subsegmental veins, which would increase the accuracy of the software. Second, this software takes an hour to emphasize the lung lobe fissures using the sheet filter method and about 20 min to interpolate the fissures by the thin plate spline method. Thus, the algorithm needs to be improved to reduce the processing time and render it a useful clinical tool. Third, the number of COPD patients in this study was relatively small; and, finally, it was a retrospective study. A prospective study with a larger number of patients is required to confirm our results. However, the aim of this study was to measure each pulmonary segment's volume based on volumetric CT data using newly developed software and to identify the differences between COPD and controls, which we achieved. We believe that this software will be useful for elucidating the clinical character of COPD. In addition, the software could be applied to evaluate the process of lung volumes in various diffuse parenchymal lung diseases in the near future.

Conclusion

The volumes of pulmonary segments based on volumetric CT data were measured using our newly developed three-dimensional software, and the differences between COPD and controls were identified. The volumes of the upper lobe segments in patients with COPD were larger than those in controls, whereas the volumes of the lower lobe segments in patients with COPD were almost the same as those in the controls.

References

1. Global Initiative for Chronic Obstructive Lung Disease (GOLD). Global strategy for the diagnosis, management, and prevention of chronic obstructive pulmonary disease. Updated 2005.
2. Goddard PR, Nicholson EM, Laszlo G, Watt I. Computed tomography in pulmonary emphysema. Clin Radiol 1982;33: 379–87.
3. Bergin C, Müller N, Nichols DM, Lillington G, Hogg JC, Mullen B, et al. The diagnosis of emphysema: a computed tomographic–pathologic correlation. Am Rev Respir Dis 1986;133:541–6.
4. Gevenois PA, De Vuyst P, Sy M, Scillia P, Chaminade L, de Maertelaer V, et al. Pulmonary emphysema: quantitative CT during expiration. Radiology 1996;199:825–9.
5. Orlandi I, Moroni C, Camiciottoli G, Bartolucci M, Pistolesi M, Villari N, et al. Chronic obstructive pulmonary disease: thin-section CT measurement of airway wall thickness and lung attenuation. Radiology 2005;234:604–10.
6. Berger P, Perot V, Desbarats P, Tunon-de-Lara JM, Marthan R, Laurent F. Airway wall thickness in cigarette smokers: quantitative thin-section CT assessment. Radiology 2005;235: 1055–64.
7. Hasegawa M, Nasuhara Y, Onodera Y, Makita H, Nagai K, Fuke S, et al. Airflow limitation and airway dimensions in chronic obstructive pulmonary disease. Am J Respir Crit Care Med 2006;173:1309–15.
8. Soejima K, Yamaguchi K, Kohda E, Takeshita K, Ito Y, Mastubara H, et al. Longitudinal follow-up study of smoking-induced lung density changes by high-resolution computed tomography. Am J Respir Crit Care Med 2000;161:1264–73.
9. Committee of Pulmonary Physiology, Japanese Respiratory Society. Guidelines for pulmonary function tests: spirometry, flow-volume curve, diffusion capacity of the lung. Tokyo: Japanese Respiratory Society; 2004 (in Japanese).
10. Nishida S, Kambe M, Sewake N, Takano M, Kawane H. Pulmonary function in healthy subjects and its prediction. 5. Pulmonary diffusing capacity in adults. *Jpn J Clin Pathol* 1976;24:941–7.
11. Sato Y, Nakajima S, Shiraga N, Atsumi H, Yoshida S, Koller T, et al. Three-dimensional multi-scale line filter for segmentation and visualization of curvilinear structures in medical images. Med Image Anal 1998;2:143–68.
12. Bookstein FL. Principal warps: thin-plate splines and decomposition of deformations. IEEE Trans Pattern Anal Mach Intell 1989;11:567–85.
13. Boztosun I, Chara A, Zerroukat M, Djidjeli K. Thin-plate spline radial basis function scheme for advection-diffusion problems. Electronic J Boundary Elements 2002;2:267–82.
14. Thurlbeck WM, Simon G. Radiographic appearance of the chest in emphysema. AJR Am J Roentgenol 1978;130: 429–40.
15. Tatsumi K, Kasahara Y, Kurosu K, Tanabe N, Takiguchi Y, Kuriyama T. Respiratory Failure Research Group in Japan. Clinical phenotypes of COPD: results of a Japanese epidemiological survey. Respirology 2004;9:331–6.
16. Kitaguchi Y, Fujimoto K, Kubo K, Honda T. Characteristics of COPD phenotypes classified according to the findings of HRCT. Respir Med 2006;100:1742–52.
17. Fujimoto K, Kitaguchi Y, Kubo K, Honda T. Clinical analysis of chronic obstructive pulmonary disease phenotypes classified using high-resolution computed tomography. Respirology 2006;11:731–40.

INTERNAL MEDICINE

□ ORIGINAL ARTICLE □

Nonspecific Interstitial Pneumonia Associated with Collagen Vascular Disease: Analysis of CT Features to Distinguish the Various Types

Tadahisa Daimon[1], Takeshi Johkoh[2], Osamu Honda[3], Hiromitsu Sumikawa[3], Kazuya Ichikado[4], Yasuhiro Kondoh[5], Hiroyuki Taniguchi[5], Kiminori Fujimoto[6], Masahiro Yanagawa[3], Atsuo Inoue[3], Noriyuki Tomiyama[3], Hironobu Nakamura[3] and Yukihiko Sugiyama[1]

Abstract

Objective The purpose of this study was to analyze the CT findings of interstitial lung diseases that are associated with collagen vascular disease (CVD), with particular attention to nonspecific interstitial pneumonia (NSIP), and to examine whether it is possible to predict the clinical diagnosis of CVDs based on the CT findings alone.

Methods CT scans of 49 patients with NSIP associated with CVD (15 males, 34 females; mean age, 55±10 years; age range, 25-76 years) were included in this retrospective study. All patients underwent a surgical biopsy. The clinical diagnosis comprised rheumatoid arthritis (RA) (n=15), systemic sclerosis (SSc) (n=8), polymyositis and dermatomyositis (PM/DM) (n=18), Sjögren's syndrome (SjS) (n=4), and mixed connective tissue disease (MCTD) (n=4). Each CT was reviewed by two independent observers who made a clinical diagnosis based on the CT findings alone.

Results The observers made a correct diagnosis for 22 (45%) of the 49 patients. A correct diagnosis was made for: RA in 7 (47%) of 15 patients; SSc in 3 (38%) of 8 patients; PM/DM in 11 (61%) of 18 patients; SjS in 1 (25%) of 4 patients. None of the 4 MCTD cases was diagnosed.

Conclusion It is difficult to make a correct clinical diagnosis of the various types of CVDs based solely on CT findings. However, it is probable to make a reasonably accurate clinical diagnosis in cases that show the typical CT findings, especially for PM/DM patients.

Key words: collagen vascular diseases, interstitial lung disease, computed tomography

(Inter Med 48: 753-761, 2009)
(DOI: 10.2169/internalmedicine.48.1714)

Introduction

Collagen vascular diseases (CVDs) constitute a group of autoimmune disorders that can involve the respiratory system and cause focal or diffuse pulmonary disease. CVDs that show radiologic features of interstitial lung disease include rheumatoid arthritis (RA), systemic lupus erythematosus (SLE), systemic sclerosis (SSc), polymyositis and dermatomyositis (PM/DM), Sjögren's syndrome (SjS), and mixed connective tissue disease (MCTD). The American Thoracic Society and European Respiratory Society defined the following seven distinct types of idiopathic interstitial pneumonia (IIP): idiopathic pulmonary fibrosis (IPF) or

[1]Department of Medicine, Division of Pulmonary Medicine, Jichi Medical University, Shimotsuke, [2]Department of Radiology, Kinki Central Hospital, Itami, [3]Department of Radiology, Osaka University Graduate School of Medicne, Suita, [4]Department of Respiratory Medicine, Saiseikai Kumamoto Hospital, Kumamoto, [5]Department of Respiratory Medicine and Allergy, Tosei General Hospital, Seto and [6]Department of Radiology, Kurume University School of Medicine, Kurume
Received for publication September 25, 2008; Accepted for publication January 28, 2009
Correspondence to Dr. Tadahisa Daimon, tada0605@jichi.ac.jp

Table 1. Demographic Data of Patients with NSIP Associated with CVD

	RA (n=15)	SSc (n=8)	PM/DM (n=18)	SjS (n=4)	MCTD (n=4)	p values
Male / female	7 / 8	3 / 5	3 / 15	1 / 3	1 / 3	0.450
Age (year)	53.5 ± 7.7	56.6 ± 12.3	54.0 ± 11.6	54.8 ± 8.2	54.5 ± 7.8	0.999
Smoking index (pack-years)	15.5 ± 12.7	24.0 ± 15.0	10.2 ± 25.8	0	0	0.102
VC (L)	2.2 ± 0.6	2.1 ± 0.7	1.7 ± 0.4	2.0 ± 0.5	1.9 ± 0.2	0.315
VC (% predicted)	71.5 ± 14.0	71.1 ± 9.3	68.4 ± 14.3	75.5 ± 21.2	76.8 ± 3.1	0.750
FEV1 (L)	1.9 ± 0.5	1.9 ± 0.8	1.5 ± 0.4	1.7 ± 0.3	1.7 ± 0.3	0.490
FEV1/ FVC (%)	86.7 ± 7.8	88.3 ± 2.5	86.2 ± 7.3	92.2 ± 6.4	89.8 ± 9.5	0.807

Note.-Data are shown as means ± SD. The data was assessed with the Kruskal–Wallis H-test.
Abbreviations: NSIP: nonspecific interstitial pneumonia, CVD: collagen vascular disease, RA: rheumatoid arthritis, SSc: systemic sclerosis, PM/DM: polymyositis and dermatomyositis, SjS: Sjögren's syndrome, MCTD: mixed connective tissue disease, VC: vital capacity, FEV1: forced expiratory volume in one second, FVC: forced vital capacity.

usual interstitial pneumonia (UIP), nonspecific interstitial pneumonia (NSIP), cryptogenic organizing pneumonia (COP) or bronchiolitis obliterans organizing pneumonia (BOOP), acute interstitial pneumonia, respiratory bronchiolitis-associated interstitial lung disease (RB-ILD), desquamative interstitial pneumonia (DIP), and lymphoid interstitial pneumonia (LIP) (1). At pathologic examination, interstitial lung diseases associated with CVD are diverse and include UIP, NSIP, COP (or BOOP), diffuse alveolar damage (DAD), and LIP (2).

Computed tomography (CT) is the most widely available, important, and standardized modality for the evaluation of interstitial lung diseases. The abnormal CT findings seen with IIPs and interstitial lung diseases associated with CVD have been extensively investigated.

Pathologic findings from patients with rheumatoid lung disease have revealed five different groups based on the specimens obtained at open lung biopsy: pulmonary rheumatoid nodules, UIP, BOOP, lymphoid hyperplasia, and NSIP (3). The CT findings reported in patients who have RA include bronchiectasis, bronchiolitis obliterans (i.e., air-trapping, mosaic perfusion), pleural effusions or pleural thickening, and enlarged lymph nodes (4).

Interstitial lung diseases associated with SLE are uncommon; in one series of 120 patients, only five (4%) had findings of interstitial lung diseases (5). The CT findings of interstitial fibrosis with SSc are similar to those of idiopathic NSIP and less extensive, less coarse, and characterized by a greater proportion of ground-glass attenuation than seen in patients with IPF (6). The types of interstitial lung diseases associated with PM/DM were identified, as follows, based on pathologic patterns: NSIP, UIP or BOOP, and DAD (7). A relatively high prevalence of consolidation (52%) and a low prevalence of honeycombing (16%) which is lower than in patients with SSc (8), were observed on high-resolution CT (HRCT) findings (9).

The common CT findings in SjS consisted of bronchiectasis and poorly defined centrilobular nodular or branching linear opacities, areas with ground-glass attenuation, and honeycombing (10). LIP frequently occurs in association with SjS, a characteristic pattern of extensive areas with ground-glass attenuation with scattered thin-walled cysts is seen in approximately 50% of LIP patients (11). The predominant abnormalities in MCTD included ground-glass attenuation, subpleural micronodules, and nonseptal linear opacities (12). The frequency of honeycombing in MCTD was lower than in SSc and higher than in PM/DM (8).

The most common type of interstitial lung disease associated with CVD is NSIP (2), followed by UIP (2). The purpose of this study was to analyze the CT findings of interstitial lung diseases associated with CVD, with particular attention to NSIP, and to examine whether it is possible to determine the clinical diagnosis of CVDs based on the CT findings alone, with particular attention to the five common CVDs, namely RA, SSc, PM/DM, SjS, and MCTD.

Methods

Study population

CT scans of 66 patients with interstitial lung diseases associated with CVD, taken between January 1995 and December 2006 at four institutions, were collected for this retrospective study. Ultimately, 49 patients with NSIP associated with CVD were enrolled. Demographic data of patients with NSIP associated with CVD are summarized in Table 1. The patients included 15 males and 34 females, aged 55±10 years (mean ± SD) (range: 25-76 years). The institutional review board gave full approval and waived informed consent for this retrospective study.

All patients underwent open lung biopsy or video-assisted thoracoscopic surgery (VATS) and all interstitial lung diseases were histologically proved at each participating institution. Biopsy specimens were obtained from 2 to 3 different lobes in each patient. The diagnosis of interstitial lung disease was based on the current histologic criteria for the diagnosis of the relevant disease by at least two experienced chest pathologists (with more than 15 years experience) (1). The clinical findings of all cases, including those from the CT, were subsequently reviewed by chest physicians. Thus, patients with infectious diseases or other types of interstitial pneumonia associated with pneumoconiosis, eosinophilic lung diseases or hypersensitivity pneumonitis were excluded. The pathological diagnoses of interstitial lung disease comprised UIP (n=12), NSIP (n=49), OP (n=1), DAD (n=2), and LIP (n=2). The clinical diagnoses of CVD with NSIP comprised RA (n=15), SSc (n=8), PM/DM (n=18), SjS (n=4), and MCTD (n=4). All four patients with SjS had primary Sjögren's syndrome.

Thin-section CT techniques

Sequential CT scans were obtained using a variety of scanners. All CT scans were performed at the end of inspiration with the patient in the supine position, and no intravenous contrast material was used. Each patient had a single chest CT examination. The CT scans consisted of 1- to 2-mm collimation sections reconstructed using a high-spatial-frequency algorithm. Images were photographed at window settings appropriate for viewing both the lung (window level from -600 to -800 HU; window width from 1,200 to 2,000 HU) and the mediastinal (window level from 20 to 80 HU; window width from 300 to 400 HU) windows. The protocols consisted of thin-sections obtained at 1-cm intervals (40 patients), 2-cm intervals (7 patients), or 3-cm intervals (2 patients).

Evaluation of thin-section CT findings

The CT scans were randomized and then retrospectively reviewed by two independent chest radiologists (O.H., H.S.). The observers knew that they were all NSIP cases associated with CVD; they were also aware of the patient's age and gender, but were unaware of any other clinical findings. The CT scans were assessed for the presence and extent of areas with ground-glass attenuation, areas of air-space consolidation, honeycombing, cysts, intralobular reticular opacity, nonseptal linear or platelike opacity, subpleural lines, thickening of bronchovascular bundles, interlobular septal thickening, centrilobular nodules, traction bronchiectasis, pleural thickening, pleural effusion, pericardial effusion, and lymph node enlargement.

Ground-glass attenuation was defined as hazy increased attenuation of the lung that did not obscure the underlying vessels (13, 14). Air-space consolidation was defined as a homogeneous increase in pulmonary parenchymal attenuation that obscured the underlying vessels (13, 14). Honeycombing was considered present when clustered cystic airspaces that ranged in size from 2 mm to 1 cm with well-defined thick walls were seen in the subpleural regions (13, 14). Cysts were defined as round airspaces with a well-defined wall (13, 14). Intralobular reticular opacity was considered present when interlacing line shadows were separated by a few millimeters (13, 14). Nonseptal linear or platelike opacity was defined as an elongated line of soft-tissue attenuation that was distinct from interlobular septa and bronchovascular bundles (13, 14). Subpleural lines were defined as a curvilinear opacity a few millimeters or less in thickness, less than 1 cm from the pleural surface and paralleling pleura (13, 14). Thickening of bronchovascular bundles was defined as an increase in bronchial wall thickness and an increase in the diameter of pulmonary artery branches caused by thickened peribronchovascular interstitium (13). Interlobular septal thickening was defined as abnormal widening of interlobular septa (13, 14). A nodule was defined as a focal, rounded opacity of less than 3 cm in diameter, which could be either well or poorly defined. When a nodule was located in the center of the lobule or lobular core, it was defined as a centrilobular nodule (13). Traction bronchiectasis was defined as irregular bronchial dilatation within or around areas with a parenchymal abnormality. Architectural distortion was considered present when bronchi, pulmonary vessels, or interlobar fissures or septa were abnormally displaced (14). Lymph nodes were considered to be enlarged if their short-axis diameter on CT exceeded 10 mm.

The lungs were divided into six zones (upper, middle, and lower zones in both lungs), and each zone was evaluated separately. The upper zone was defined as the part of the lung above the level of the tracheal carina; the lower zone, as the part of the lung below the level of the inferior pulmonary vein; and the middle zone, as the portion of the lung between the upper and lower zones. Each CT finding was assessed and considered present, and the extent of involvement of the findings was evaluated visually and independently for each lung zone. A score was assigned on the basis of the percentage of lung parenchyma that showed evidence of an abnormality and was estimated to the nearest 10% of parenchymal involvement. The overall percentage of involvement was calculated by averaging the scores of the six lung zones.

The extent of traction bronchiectasis was evaluated by counting the number of segments that showed evidence of traction bronchiectasis. The following 18 segments or subsegments were evaluated: right apical upper, right anterior upper, right posterior upper, right lateral middle, right medial middle, right superior upper, right medial basal, right anterior basal, right lateral basal, right posterior basal, left apicoposterior upper, left anterior upper, left superior lingular, left inferior lingular, left superior lower, left anteromedial basal, left lateral basal, and left posterior basal. The extent of traction bronchiectasis was also quantified by assessing the generations of the most proximal bronchial branches involved. Traction bronchiectasis was scored as follows: 0, no bronchial dilatation; 1, bronchial dilatation involving bronchi distal to the fourth-generation bronchi; 2, bronchial dilatation involving from the second- and third-generation bronchi; 3, bronchial dilatation involving the trachea and/or the main bronchus.

After assessing the presence and extent of findings, the observers evaluated their predominant distribution. Zonal predominance was assessed as being upper or lower. Upper lung zone predominance was present when most of the abnormalities were above the level of the tracheal carina; and lower zone predominance was present when most of the abnormalities were below this level. The anatomic distribution was noted to be central if the abnormalities were primarily located in the inner third of the lung, and peripheral if the abnormalities were primarily present in the outer third of the lung. Peribronchovascular predominance was defined as findings located mainly around the bronchus and artery.

After reviewing the thin-section CT findings, the observers recorded the clinical diagnosis of CVDs, as suggested by

Table 2. Summary of CT Findings of Each Interstitial Lung Diseases Associated with CVD

Diagnosis	CT findings
RA	Intralobular reticular opacity, honeycombing, lower lung zone and posterior predominance. Bronchiectasis, centrilobular nodules. Pleural effusions or pleural thickening, and enlarged lymph nodes.
SSc	Intralobular reticular opacity similar to those of idiopathic NSIP and less extensive, less coarse. Ground-glass attenuation, air-space consolidation, lower lung zone and posterior predominance.
PM/DM	Air-space consolidation, a low prevalence of honeycombing (lower than SSc), lower lung zone and posterior predominance. Nonseptal linear or platelike, subpleural lines.
SjS	Bronchiectasis, centrilobular nodules, thickening of bronchovascular bundles. Ground-glass attenuation with scattered thin-walled cysts.
MCTD	A combination of those seen in SLE, SSc, and PM/DM. Ground-glass attenuation, air-space consolidation, honeycombing (lower than SSc and higher than PM/DM). Pleural effusions or pleural thickening.

Note. The descriptions of CT findings are based on information from references 3-15.
Abbreviations: CT: computed tomography, CVD: collagen vascular disease, RA: rheumatoid arthritis, SSc: systemic sclerosis, PM/DM: polymyositis and dermatomyositis, SjS: Sjögren's syndrome, MCTD: mixed connective tissue disease.

the CT findings according to previously published data of each interstitial lung diseases associated with CVD (Table 2). Differential diagnosis was limited to the five types (RA, SSc, PM/DM, SjS, and MCTD).

Statistical analysis

All statistical analyses were performed using statistical software (SPSS, version 12.0J; SPSS, Tokyo, Japan). The inter-observer variation for the extent of various abnormalities was analyzed using the Bland-Altman plot. The inter-observer variation for the clinical diagnosis of CVDs based on CT findings was analyzed with the κ statistic. Inter-observer agreement was classified as poor (κ=0.00-0.20), fair (κ=0.21-0.40), moderate (κ=0.41-0.60), good (κ=0.61-0.80), or excellent (κ=0.81-1.00). Statistical significance was defined as $p<0.05$.

The readings of the two observers pertaining to the extent of various abnormal findings were combined by calculating the average. Disagreement regarding the existence of pleural thickening, pleural effusion, pericardial effusion, lymph node enlargement, the anatomic distribution, the zonal predominance, and the clinical diagnosis of CVDs based on the CT findings was resolved by the consensus of the two observers.

The Kruskal-Wallis *H*-test was used to evaluate differences in the demographic data of patients, the extent of various abnormalities, pleural thickening, pleural effusion, pericardial effusion, lymph node enlargement, the anatomic distribution, and the zonal predominance between each NSIP associated with CVD. A post-hoc test (Tukey's HSD procedure) was used to evaluate differences between each set of two groups.

Results

Observer agreement

Inter-observer agreement for the clinical diagnosis of CVDs based on CT findings was fair (κ=0.28).

The result of the Bland-Altman plot between the two observers is shown in Fig. 1. The x-axis of this graph is the average of two results for the extent of various abnormalities. The y-axis represents the difference between two results for the extent of various abnormalities. This assay indicates the inter-observer agreement of the extent of various abnormalities, if each plot existed within the bound of the average ±2 × SD of difference of two results. The SD was 2.6 (2 SD=5.2), and the average was 0.3 (%) (Fig. 1).

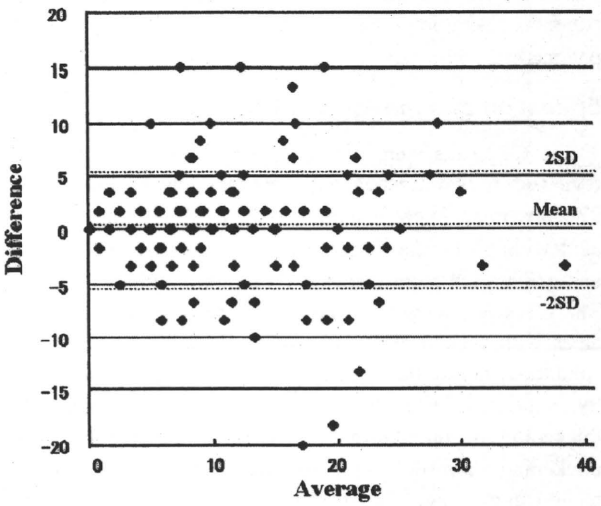

Figure 1. Bland-Altman plot of the extent of various abnormalities. This graph was plotted to compare two results of the extent of various abnormalities (Horizontal axis: the average of two results, Vertical axis: the difference of two results).

Diagnosis

The observers made a correct diagnosis for 22 (45%) of the 49 patients, as summarized in Table 3. A correct diagnosis of RA was made for 7 (47%) of 15 patients (Figs. 2-4); of the 8 RA cases misdiagnosed by the observer, 3 were incorrectly recorded as SSc and 5 as PM/DM. A correct diagnosis of SSc was made for 3 (38%) of 8 patients (Figs. 5-7); of the 5 misdiagnosed SSc cases, the observer recorded 4 as RA and 1 as PM/DM. A correct diagnosis of PM/DM was made for 11 (61%) of 18 patients (Figs. 8, 9); of the 7 misdiagnosed PM/DM cases, the observer recorded 5 as RA and 2 as SSc. A correct diagnosis of SjS was made

Figure 2. Nonspecific interstitial pneumonia (NSIP) associated with RA in a 63-year-old man. Transverse thin-section CT (2-mm collimation) at the level of tracheal carina demonstrates areas of air-space consolidation with traction bronchiectasis (large arrows) in a predominantly peribronchovascular distribution, and extensive diffusely distributed centrilobular nodules (small arrows).

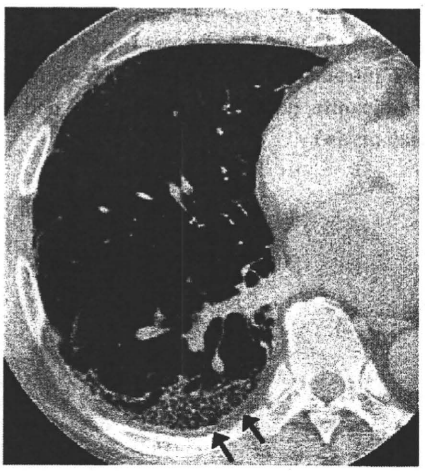

Figure 3. Nonspecific interstitial pneumonia (NSIP) associated with RA in a 54-year-old man. Transverse thin-section CT (1-mm collimation) at the level of the right inferior pulmonary vein demonstrates intralobular reticular opacity (arrows) with a predominantly peripheral distribution.

for 1 (25%) of 4 patients (Fig. 10). None of the 4 MCTD cases was diagnosed based on CT findings alone (Fig. 11).

Extent and distribution of CT findings

Significant differences in the extent of various abnormalities between each patient with NSIP associated with CVD were found with honeycombing (p=0.014), cysts (p=0.030), intralobular reticular opacity (p=0.007), subpleural lines (p=0.002), and interlobular septal thickening (p=0.042) (Table 4).

Among patients with NSIP associated with CVD, areas with ground-glass attenuation were present in all types of

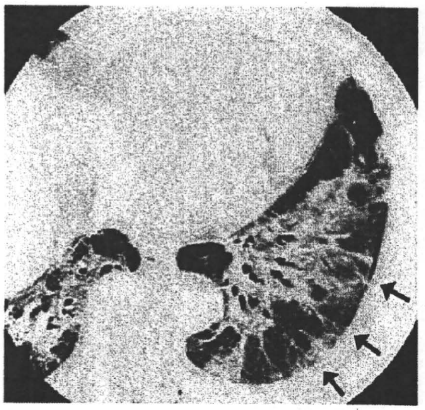

Figure 4. Nonspecific interstitial pneumonia (NSIP) associated with RA in a 55-year-old woman. Transverse thin-section CT (2-mm collimation) through the left lower lobe demonstrates areas of air-space consolidation (arrows) with a predominantly peribronchovascular distribution.

Figure 5. Nonspecific interstitial pneumonia (NSIP) associated with SSc in a 42-year-old man. Transverse thin-section CT (1-mm collimation) through the lower lobes demonstrates intralobular reticular opacity (arrows) with a predominantly peripheral distribution.

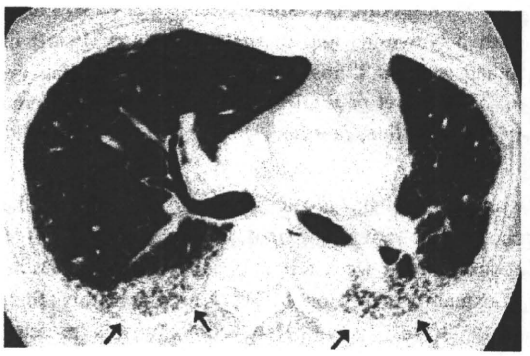

Figure 6. Nonspecific interstitial pneumonia (NSIP) associated with SSc in a 52-year-old woman. Transverse thin-section CT (2-mm collimation) at the level of the right superior pulmonary vein demonstrates areas of air-space consolidation (arrows) with a predominantly peripheral distribution.

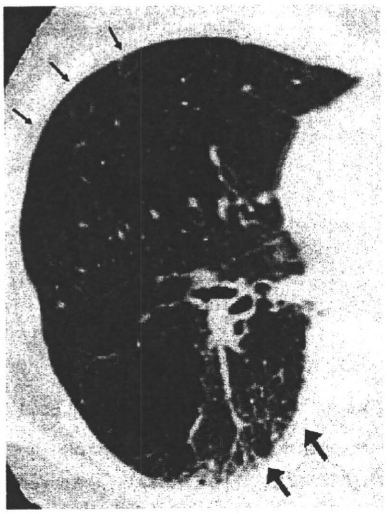

Figure 7. Nonspecific interstitial pneumonia (NSIP) associated with SSc in a 67-year-old woman. Transverse thin-section CT (1-mm collimation) at the level of the right inferior pulmonary vein demonstrates intralobular reticular opacity (large arrows) witha predominantly peribronchovascular distribution and extensive diffusely distributed centrilobular nodules (small arrows).

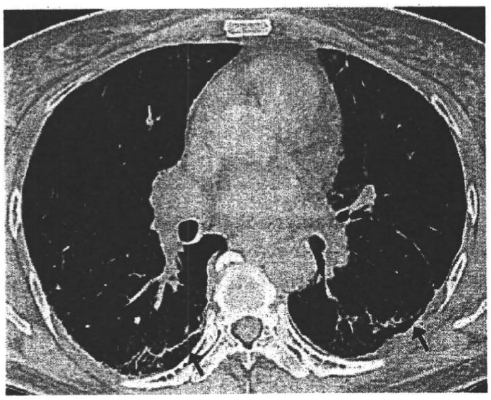

Figure 8. Nonspecific interstitial pneumonia (NSIP) associated with polymyositis and dermatomyositis (PM/DM) in a 51-year-old woman. Transverse thin-section CT(2-mm collimation) at the level of the inferior pulmonary vein demonstratessubpleural lines (arrows).

CVDs and showed the greater extent in SSc, although the differences were not significant (p=0.369). Areas of airspace consolidation were found in all types of CVDs with similar extent, except for MCTD in which this finding showed the lowest extent. Honeycombing was present in four types of CVDs, except for SjS. The extent of honeycombing in MCTD was significantly greater than those in SSc (p=0.050). The extent of honeycombing in SSc was less than in RA and PM/DM, but there were no significant differences (p=0.853, 0.895). Cysts were present in PM/DM, SjS, and MCTD with similar extent. Intralobular reticular opacity was present in all types of CVDs. The extent of intralobular reticular opacity in SSc was significantly greater than in RA (p=0.007) and PM/DM (p=0.029) (Fig. 5). Nonseptal linear or platelike opacity was present in all types of CVDs, but with no significant differences (p=0.701). Subpleural lines were found in all types. The extent of subpleural lines in PM/DM was significantly greater than those in RA (p=0.024) and SSc (p=0.017) (Fig. 8). The extent of subpleural lines in MCTD was also greater than others, but there were no significant differences (Fig. 11). Interlobular

Figure 9. Nonspecific interstitial pneumonia (NSIP) associated with PM/DM in a 51-year old woman. Transverse thin-section CT (2-mm collimation) through the left lower lobe demonstrates intralobular reticular opacity (large arrows) with apredominantly peripheral distribution and platelike opacity (small arrow).

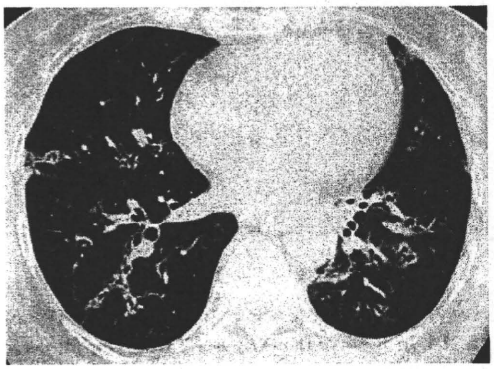

Figure 10. Nonspecific interstitial pneumonia (NSIP) associated with SjS in a 62-year old woman. Transverse thin-section CT (1-mm collimation) at the level of the inferior pulmonary vein demonstrates intralobular reticular opacity with traction bronchiectasis (arrows) with a predominantly peribronchovascular distribution.

septal thickening was found in all types. The extent of interlobular septal thickening in SjS was significantly greater than in RA (p=0.050). Centrilobular nodules were present in RA, SSc, and PM/DM, and showed a greater extent in RA (Fig. 2), although the differences were not significant. Traction bronchiectasis was present in all types, but with no significant difference.

Pleural thickening and lymph node enlargement were present in all types, and the differences were not significant. Pleural effusion was present in SSc, PM/DM, and SjS, with no significant differences. Pericardial effusion was absent in all types (Table 4).

The incidence of patients with RA and SjS with a lower zonal predominance was less than for the other 3 types (p= 0.001) (Table 4). There were no significant differences in anatomic distribution among patients with NSIP associated with CVD.

Discussion

The observers made a correct diagnosis for 22 (45%) of the 49 patients. A correct diagnosis was made for: RA in 7 (47%) of 15 patients; SSc in 3 (38%) of 8 patients; PM/DM in 11 (61%) of 18 patients; and SjS in 1 (25%) of 4 patients. None of the 4 MCTD cases was diagnosed based on CT findings alone.

Figure 11. Nonspecific interstitial pneumonia (NSIP) associated with mixed connective tissue disease (MCTD) in a 45-year-old woman. Transverse thin-section CT (1-mm collimation) at the level of the right inferior pulmonary vein demonstrates intralobular reticular opacity (large arrows) with a predominantly peripheral distribution and subpleural lines (small arrows).

The types of interstitial lung diseases associated with PM/DM were identified on the basis of pathologic patterns: NSIP, UIP or BOOP, and DAD (7). The frequency of honeycombing was 16% of patients who had abnormal HRCT findings (9), which is lower than in patients with SSc (8). In the present study, the extent of honeycombing in patients with NSIP with PM/DM was not significantly different from each other (Table 4). The extent of intralobular reticular opacity was less than in patients with NSIP with SSc, while it was also almost the same as in patients with NSIP with RA (Table 4). Nonseptal linear or plate-like opacity has been reported as one of the most common CT findings in interstitial lung diseases associated with PM/DM (9, 15). In the present study, in patients with NSIP with PM/DM, nonseptal linear or plate-like opacity was present in 7 (39%) of 18 patients (Fig. 9).

Subpleural lines were defined as a curvilinear opacity, which was also termed a subpleural curvilinear shadow, a few millimeters or less in thickness, less than 1 cm from the pleural surface and paralleling pleura (13, 14). It was first described in patients with asbestosis. This occurs as a result of atelectasis, fibrosis, or inflammation, and can be seen in a variety of lung diseases including IPF or UIP (16), as well as in normal patients as a result of atelectasis. Schurawitzki et al reported that 17 (74%) of 23 patients with SSc showed subpleural lines on HRCT (17). Mino et al reported that 7 (38%) of 19 patients with PM/DM showed subpleural lines on HRCT (18). In the present study, subpleural lines were present in: 12 (67%) of 18 NSIP cases with PM/DM; 4 (27%) of 15 NSIP cases with RA; 2 (15%) of 8 NSIP cases with SSc; 1 (25%) of 4 NSIP cases with SjS; and 2 (50%) of 4 NSIP cases with MCTD. Subpleural lines were therefore most commonly found in patients with NSIP with PM/DM (Fig. 8). This information may be useful in the diagnosis of interstitial lung diseases associated with PM/DM.

Pulmonary parenchymal abnormalities are more common and more severe in SSc than in the other types of CVD. The pathologic features are of NSIP or UIP, the former being more common (7). The CT findings of interstitial fibrosis with SSc are similar to those of idiopathic NSIP and less extensive, less coarse, and characterized by a greater proportion of ground-glass attenuation than seen in patients with IPF (6). In the present study, in NSIP patients with SSc, the extent of intralobular reticular opacity was significantly greater than those in RA (p=0.007) and PM/DM (p=0.029) (Table 4). The abnormalities showed lower lung zone and posterior predominance, which is the same as in a previous report (6) (Figs. 5, 6). This might be useful information for

Table 3. Clinical Diagnosis of NSIP Associated with CVD Based on CT Findings

	RA (n=15)	SSc (n=8)	PM/DM (n=18)	SjS (n=4)	MCTD (n=4)	Total (n=49)
Number (%)	7 (47)	3 (38)	11 (61)	1 (25)	0 (0)	22 (45)

Note. Data in parentheses are percentages.

Abbreviations: NSIP: nonspecific interstitial pneumonia, CVD: collagen vascular disease, CT: computed tomography, RA: rheumatoid arthritis, SSc: systemic sclerosis, PM/DM: polymyositis and dermatomyositis, SjS: Sjögren's syndrome, MCTD: mixed connective tissue disease.

Table 4. Extent and Distribution of Thin-section CT Findings of Each NSIP Associated with CVD

CT finding	RA (n=15) Extent	SSc (n=8) Extent	PM/DM (n=18) Extent	SjS (n=4) Extent	MCTD (n=4) Extent	p values
Ground-glass attenuation*	14.2 ± 9.0	17.4 ± 7.2	15.1 ± 7.8	11.5 ± 3.5	16.3 ± 13.5	0.369
Air-space consolidation*	7.7 ± 6.8	6.0 ± 6.2	5.2 ± 4.1	7.3 ± 4.4	2.1 ± 2.5	0.157
Honeycombing*	1.4 ± 3.1	0.2 ± 0.8 [‖]	1.3 ± 4.7	0	4.8 ± 4.1 [‖]	0.014§
Cysts*	0 [‖]	0	0.4 ± 1.2	0.4 ± 0.7	1.0 ± 1.7 [‖]	0.030§
Intralobular reticular opacity*	3.3 ± 6.0	9.8 ± 5.4 [‖]	4.4 ± 3.9 [¶]	2.9 ± 2.5	5.8 ± 7.2	0.007§
Nonseptal linear or platelike opacity*	1.4 ± 2.3	1.0 ± 2.1	1.6 ± 2.1	1.5 ± 2.4	1.9 ± 2.2	0.701
Subpleural lines*	0.9 ± 2.0	1.2 ± 2.2 [‖]	2.7 ± 2.1 [¶]	1.4 ± 2.4	2.9 ± 2.5	0.002§
Thickening of bronchovascular bundles*	0.2 ± 0.8	0.4 ± 1.1	0.3 ± 0.9	0	0.4 ± 1.1	0.222
Interlobular septal thickening*	0.2 ± 0.7	1.5 ± 3.2	0.6 ± 1.4	2.3 ± 2.0 [¶]	1.0 ± 1.7	0.042§
Centrilobular nodules*	1.4 ± 3.1	0.6 ± 1.4	0.1 ± 0.4	0	0	0.189
Generations of traction bronchiectasis†	1.5 ± 0.5	1.3 ± 0.5	1.3 ± 0.5	1.3 ± 0.5	1.0 ± 0	0.075
No.of segments with traction bronchiectasis	10.8 ± 3.8	11.4 ± 3.2	9.9 ± 3.0	8.8 ± 4.5	11.0 ± 4.8	0.206
No.of patients with pleural thickening‡	3 (20)	4 (50)	9 (50)	1 (25)	2 (50)	0.181
No.of patients with pleural effusion‡	0 (0)	2 (25)	3 (17)	1 (25)	0 (0)	0.159
No.of patients with pericardial effusion‡	0 (0)	0 (0)	0 (0)	0 (0)	0 (0)	NA
No.of patients with lymph node enlargement‡	4 (27)	2 (25)	2 (11)	1 (25)	1 (25)	0.505
Zonal predominance						
No.of patients with upper predominance‡	3 (20)	1 (13)	0 (0)	1 (25)	0 (0)	0.062
No.of patients with lower predominance‡	10 (67) [‖]	7 (88)	17 (94)	2 (50)	4 (100) [¶]	0.001§
Anatomic distribution						
No.of patients with central predominance‡	0 (0)	0 (0)	0 (0)	0 (0)	0 (0)	NA
No.of patients with peripheral predominance‡	8 (53)	3 (38)	9 (50)	2 (50)	3 (75)	0.850
No.of patients with peribronchovascular predominance‡	13 (87)	7 (88)	17 (94)	3 (75)	4 (100)	0.230

Note. -Unless otherwise indicated, data are mean ± standard deviation. The data was assessed with the Kruskal–Wallis H-test. NA = not available

* Data are percentage of lung parenchyma.

† Data are scores.

‡ Data in parentheses are percentages.

identifying interstitial lung diseases associated with SSc. However, there were some SSc cases with combined centrilobular nodules that the observers incorrectly recorded as RA (Fig. 7). It is difficult to clearly distinguish the clinical diagnosis of SSc from the other types based solely on CT findings.

In NSIP patients with RA, the extent of honeycombing was not significantly different from each other (Table 4). The extent of intralobular reticular opacity in RA was significantly less than those in SSc (p=0.007). The extent of centrilobular nodules in RA was not significantly different from each other (Table 4). In the present study, pleural effusion was not present in patients with NSIP with RA. Pleural thickening was present in 3 (20%) of 15 RA patients with NSIP. Lymph node enlargement was present in 4 patients (27%). Patterns of CT findings from NSIP cases with RA were diverse (Figs. 2-4) and there were no characteristic CT findings of NSIP with RA to allow differentiation from the other 4 types with NSIP.

Sjögren's syndrome can occur as a primary disease, without features of other CVD, or as a secondary disease in association with other CVDs, most commonly RA. LIP frequently occurs in association with SjS, followed in frequency by airway abnormalities such as follicular bronchitis, bronchiectasis, and bronchiolitis (7). A characteristic pattern of extensive areas with ground-glass attenuation with scattered thin-walled cysts is seen in approximately 50% of patients with LIP (19). Poorly defined centrilobular nodules and thickening of the bronchovascular bundles, also seen in LIP, represent expansion of the interstitial tissue by lymphoplasma cell infiltration (19). In the present study, cysts were seen in NSIP patients with SjS, but the extent of cysts was not significantly different from each other (Table 4). Honeycombing, thickening of bronchovascular bundles and centrilobular nodules were not seen in NSIP patients with SjS (Table 4).

Based on the findings of this study and previous reports (8, 12), CT findings of NSIP associated with MCTD resemble NSIP with PM/DM (Fig. 11). Saito et al (8) also concluded that CT findings in MCTD were a combination of those seen in other patients (SLE, SSc, and PM/DM). In the present study, 4 MCTD cases were recorded incorrectly as RA (n=2), SSc (n=1), and PM/DM (n=1). Indeed, it is difficult to define the clinical diagnosis of MCTD based on the CT findings alone.

The present study has several limitations. First, the number of patients with NSIP associated with SjS and MCTD was relatively small. Second, patients with interstitial lung diseases associated with SLE were not included. Interstitial lung diseases associated with SLE are rare, and this limitation must be reflected in clinical practice. Third, this was a retrospective study and thus a prospective study is required to confirm the results. Finally, the CT images used in this study were obtained using different CT scanners and proto-

cols, and thus the details of each finding could be evaluated only to a limited degree.

In conclusion, generally speaking, it is difficult to arrive at a correct clinical diagnosis of CVDs based on CT findings alone. However, it is probable to make a reasonably accurate clinical diagnosis in cases that show the typical CT findings, especially for PM/DM patients. Using the detailed findings on HRCT, a feasible method to predict the diagnosis of NSIP-associated CVD.

Acknowledgement

This study was supported by the Health and Labor Sciences Research Grants on Diffuse Lung Diseases from the Japanese Ministry of Health, Labor and Welfare.

References

1. American Thoracic Society, European Respiratory Society. American Thoracic Society/European Respiratory Society International Multidisciplinary Consensus Classification of the Idiopathic Interstitial Pneumonias: this joint statement of the American Thoracic Society (ATS), and the European Respiratory Society (ERS) was adopted by the ATS Board of Directors, June 2001 and by the ERS Executive Committee, June 2001. Am J Respir Crit Care Med **165**: 277-304, 2002.
2. Tansey D, Wells AU, Colby TV, et al. Variations in histological patterns of interstitial pneumonia between connective tissue disorders and their relationship to prognosis. Histopathology **44**: 585-596, 2004.
3. Yousem SA, Colby TV, Carrington CB. Lung biopsy in rheumatoid arthritis. Am Rev Respir Dis **131**: 770-777, 1985.
4. Remy-Jardin M, Remy J, Cortet B, Mauri F, Delcambre B. Lung changes in rheumatoid arthritis: CT findings. Radiology **193**: 375-382, 1994.
5. Haupt HM, Moore GW, Hutchins GM. The lung in systemic lupus erythematosus: analysis of the pathologic changes in 120 patients. Am J Med **71**: 791-798, 1981.
6. Desai SR, Veeraraghavan S, Hansell DM, et al. CT features of lung disease in patients with systemic sclerosis: comparison with idiopathic pulmonary fibrosis and nonspecific interstitial pneumonia. Radiology **232**: 560-567, 2004.
7. Kim EA, Lee KS, Johkoh T, et al. Interstitial lung diseases associated with collagen vascular diseases: radiologic and histopathologic findings. Radiographics **22**: 151-165, 2002.
8. Saito Y, Terada M, Takada T, et al. Pulmonary involvement in mixed connective tissue disease: comparison with other collagen vascular diseases using high resolution CT. J Comput Assist Tomogr **26**: 349-357, 2002.
9. Ikezoe J, Johkoh T, Kohno N, Takeuchi N, Ichikado K, Nakamura H. High-resolution CT findings of lung disease in patients with polymyositis and dermatomyositis. J Thorac Imaging **11**: 250-259, 1996.
10. Franquet T, Gimenez A, Monill JM, Diaz C, Geli C. Primary Sjogren's syndrome and associated lung disease: CT findings in 50 patients. AJR Am J Roentgenol **169**: 655-658, 1997.
11. Koyama M, Johkoh T, Honda O, et al. Pulmonary involvement in primary Sjogren's syndrome: spectrum of pulmonary abnormalities and computed tomography findings in 60 patients. J Thorac Imaging **16**: 290-296, 2001.
12. Kozuka T, Johkoh T, Honda O, et al. Pulmonary involvement in mixed connective tissue disease: high-resolution CT findings in 41 patients. J Thorac Imaging **16**: 94-98, 2001.
13. Webb WR, Müller NL, Naidich DP. High-resolution computed tomography findings of lung disease. High-resolution CT of the lung. 3rd ed. Lippincott Williams & Wilkins, Philadelphia, 2001: 71-192.
14. Austin JH, Müller NL, Friedman PJ, et al. Glossary of terms for CT of the lungs: recommendations of the Nomenclature Committee of the Fleischner Society. Radiology **200**: 327-331, 1996.
15. Douglas WW, Tazelaar HD, Hartman TE, et al. Polymyositis-dermatomyositis-associated interstitial lung disease. Am J Respir Crit Care Med **164**: 1182-1185, 2001.
16. al-Jarad N, Strickland B, Pearson MC, Rubens MB, Rudd RM. High resolution computed tomographic assessment of asbestosis and cryptogenic fibrosing alveolitis: a comparative study. Thorax **47**: 645-650, 1992.
17. Schurawitzki H, Stiglbauer R, Graninger W, et al. Interstitial lung disease in progressive systemic sclerosis: high-resolution CT versus radiography. Radiology **176**: 755-759, 1990.
18. Mino M, Noma S, Taguchi Y, Tomii K, Kohri Y, Oida K. Pulmonary involvement in polymyositis and dermatomyositis: sequential evaluation with CT. Am J Roentgenol **169**: 83-87, 1997.
19. Johkoh T, Muller NL, Pickford HA, et al. Lymphocytic interstitial pneumonia: thin-section CT findings in 22 patients. Radiology **212**: 567-572, 1999.

Eur Respir J 2009; 33: 1415–1428
DOI: 10.1183/09031936.00084307

Interleukin-1 receptor-related protein ST2 suppresses the initial stage of bleomycin-induced lung injury

N. Mato*, M. Fujii#, Y. Hakamata¶, E. Kobayashi+, A. Sato§, M. Hayakawa#, H. Ohto-Ozaki#, M. Bando*, S. Ohno*, S. Tominaga# and Y. Sugiyama*

ABSTRACT: Acute lung injury has a range of causes, and occasionally leads to lethal respiratory failure. Despite advances in treatment, acute lung injury continues to have a high mortality rate, and thus a new therapeutic approach is needed. ST2 is an interleukin (IL)-1 receptor-related protein, and its expression is induced by various inflammatory responses. Recently, ST2 has been speculated to exert anti-inflammatory effects; therefore, we investigated the role of the ST2 in the murine model of acute lung injury.

To elucidate the function of ST2 *in vivo*, mice that transiently overexpressed ST2 protein were prepared using the hydrodynamic gene transfer method, and lung injury was induced by intratracheal administration of bleomycin.

In bleomycin-treated ST2-overexpressing mice, the increase of neutrophils in the bronchoalveolar lavage fluid (BALF) was markedly suppressed. Additionally, the levels of tumour necrosis factor-α and IL-6, as well as the concentration of albumin, in BALF were reduced compared with those of controls. Furthermore, the pulmonary architecture in ST2-overexpressing mice remained almost normal, and the survival rate was significantly improved.

From these results, we concluded that ST2 has the potential to suppress the initial stage of acute lung injury, and therefore it may be a useful reagent for the treatment of acute lung injury.

KEYWORDS: Acute lung injury, bleomycin, hydrodynamic injection, ST2

Acute lung injury (ALI) can be triggered by various stimuli, including drugs, sepsis and trauma [1]. It is characterised by epithelial and endothelial damage, and is followed by destruction of the alveolar capillary–epithelial barrier. The increased permeability of pulmonary capillary vessels allows flooding of inflammatory cells, enables plasma proteins to enter the lung and results in a disturbance of gas exchange [1, 2]. The mortality rate of ALI patients remains high (40–60%) despite the numerous attempts that have been made to develop new therapies [2]. For the treatment of ALI, factors such as mechanical ventilation settings, oxygen concentration maintenance and the management of fluid balance have been extensively investigated, and new devices and techniques have led to important improvements. However, in spite of these efforts, an effective therapy to attenuate the inflammatory process in ALI has not been established.

TOMINAGA [3] originally identified the ST2 (interleukin (IL)-1 receptor-related) gene as an early-response gene in mouse fibroblasts. The ST2 gene generates at least four different gene products, the soluble secreted form (ST2), the transmembrane form (ST2L) and two variant forms (ST2V and ST2LV), by alternative splicing [4]. Recently, a specific ligand for ST2L was discovered and named IL-33 by SCHMITZ *et al.* [5]. ST2 has been known to be related to various disorders in humans and an increase of serum ST2 has been reported in conditions such as septic shock [6], severe trauma [6], bronchial asthma [7] and idiopathic pulmonary fibrosis, especially in acute exacerbation [8]. Several experimental studies have suggested that the induction of ST2 by various inflammatory stimuli may confer protection against inflammatory damage. For example, it has been reported that pre-treatment with ST2 resulted in an attenuation of pro-inflammatory cytokines and an enhanced survival rate in a

AFFILIATIONS
*Division of Pulmonary Medicine, Dept of Medicine, Jichi Medical University,
#Dept of Biochemistry, Jichi Medical University,
+Division of Organ Replacement Research, Center for Molecular Medicine, Jichi Medical University, and,
§Dept of Dermatology, Jichi Medical University, Tochigi, and
¶Dept of Basic Science, School of Veterinary Nursing and Technology, Nippon Veterinary and Life Science University, Musashino-shi, Japan.

CORRESPONDENCE
Y. Sugiyama
Division of Pulmonary Medicine,
Jichi Medical University,
3311-1 Yakushiji,
Shimotsuke-Shi,
Tochigi 329-0498,
Japan.
Fax 81 285443586
E-mail: sugiyuki@jichi.ac.jp

Received:
July 07 2007
Accepted after revision:
January 13 2009

SUPPORT STATEMENT
The present study was supported in part by a grant from the Center of Excellence in the 21st Century Program of the Ministry of Education, Culture, Sports, Science, and Technology of Japan (Tokyo, Japan).

STATEMENT OF INTEREST
None declared.

European Respiratory Journal
Print ISSN 0903-1936
Online ISSN 1399-3003

This article has supplementary material accessible from www.erj.ersjournals.com

mouse endotoxin shock model [9]. ST2 has also been shown to inhibit degradation of inhibitor on nuclear factor-κB and suppress lipopolysaccharide-induced IL-6 production in THP-1 cells [10]. Additionally, in a collagen-induced arthritis model, it was demonstrated that ST2 suppressed the production of inflammatory cytokines and significantly attenuated the disease [11].

Taken together, these findings suggest that it is worthwhile to assess the therapeutic potential of ST2 as an anti-inflammatory agent *in vivo*. In the current study, ST2-overexpressing mice were prepared by the hydrodynamic gene transfer method, and the effects of ST2 on bleomycin-induced lung injury were investigated. Based on the anti-inflammatory effects of ST2, it was hypothesised that its *in vivo* overexpression would ameliorate bleomycin-induced lung injury in mice.

MATERIALS AND METHODS

Mice

Male C57BL/6 mice, aged 7–8 weeks (body weight 18–22 g), were purchased from Japan SLC (Hamamatsu, Japan). Mice were maintained under standard conditions and fed rodent chow and water *ad libitum*. The research proposal was reviewed by the animal ethical committee of Jichi Medical University (permission No. 152; Tochigi, Japan), and all experiments were performed in accordance with the Jichi Medical University Guide for Laboratory Animals, based on the Helsinki convention for the use and care of animals. The number of mice employed in the different experiments is described in the relevant figure legends.

Plasmids

pCAGGS and pCAGGS-LacZ were kindly provided by J. Miyazaki (Osaka University, Osaka, Japan) and T. Murakami (Jichi Medical University, Tochigi, Japan), respectively. pCAGGS was an efficient expression vector driven by the chicken β-actin promoter, and pCAGGS-LacZ was constructed by insertion of the β-galactosidase reporter gene into pCAGGS. pCAGGS-mST2 was constructed by insertion of mouse ST2 (mST2) cDNA into the Xho1 restriction site of pCAGGS. The European Molecular Biology Laboratory/GeneBank accession number for the nucleotide sequence mST2 is Y07519. mST2 cDNA was originally isolated from the cDNA library of BALB/c-3T3 cells after growth stimulation with serum [12]. First, the Hinc 2 fragment of mST2 cDNA containing the entire coding region (1,582 bp) was inserted into the Xba1 site of the pEF-BOS plasmid (pEF-BOS-mST2) using an Xba1 linker. Secondly, the fragment of mST2 was obtained from pEF-BOS-mST2 by digestion with Xba1, and ligated with the Xho1 linker. Thirdly, the pCAGGS plasmid was digested with Xho1 and finally the mST2 fragment, digested with Xho1, was inserted. Plasmids were purified with a Plasmid Maxi Kit (Qiagen, Valencia, CA, USA). The pGL3 control vector containing a firefly luciferase reporter gene was purchased from Promega (Madison, WI, USA).

Cell culture and in vitro transfection

To confirm that the constructed plasmid was appropriate for producing soluble recombinant ST2 protein, human embryonic kidney (HEK) 293T cells were cultured and transfected with pCAGGS and pCAGGS-mST2. HEK 293T cells were kindly provided by T. Kasahara (Kyoritsu University of Pharmacy, Tokyo, Japan), and were cultured in Dulbecco's modified Eagle's medium (Sigma-Aldrich, St Louis, MO, USA) containing 10% (volume/volume (v/v)) foetal bovine serum (Thermo Trace, Melbourne, Australia). The amount of plasmid was 10 μg, and transfection was carried out by the calcium phosphate precipitation method.

Western blotting

20 h after the transfection of pCAGGS and pCAGGS-mST2, the culture medium was collected, digested with *N*-Glycosidase-F (Roche, Indianapolis, IN, USA), and subjected to sodium dodecyl sulphate-polyacrylamide gel electrophoresis and immnunoblotting, as described previously [12]. In brief, proteins were separated electrophoretically with 10% polyacrylamide gel and transferred to an Immobilon-P membrane (Millipore, Bedford, MA, USA) at 100 mA for 1 h. Immunoblotting was performed with rabbit anti-mouse ST2 polyclonal antibody (×1000 dilution) against the recombinant ST2 protein from *Escherichia coli*, and after incubation for 1 h at room temperature. Then the membrane was incubated for 0.5 h with anti-rabbit immunoglobulin (Ig) G-horseradish peroxidase (HRP; ×5000 dilution; Jackson Immunoresearch, West Grove, PA, USA) as a secondary antibody, and the protein band was visualised by the ECL system (Amersham Bioscience, Amersham, UK).

In vivo *gene transfer*

Plasmid vectors were delivered into mice by hydrodynamic injection, which is an efficient *in vivo* method of gene transfer. Plasmid DNA was diluted in sterile saline, and the final volume was adjusted to 6.3% of total body weight [13]. Under mild anesthesia with diethyl ether, mice were injected with the plasmid solution through the dorsal penile vein in 5–8 s, using a 26-gauge needle. The amount of plasmid vector was appropriately chosen in each experiment.

To evaluate liver damage, mice were sacrificed and blood was collected at 24 and 48 h after the hydrodynamic gene transfer. Serum aspartate aminotransferase (AST) and alanine aminotransferase (ALT) levels were assayed by the Japan Society of Clinical Chemistry transferase method using an AST kit and ALT kit (Wako, Osaka, Japan) by the Clinical Analyzer Model 7180 (Hitachi High-Technologies Co., Tokyo, Japan).

In vivo *bioluminescent imaging and luciferase asssay*

In order to examine the expression and distribution of the transgene after hydrodynamic injection, *in vivo* bioimaging was performed. Mice were injected with 20 μg of pGL3 control vector or saline as a control, and 24 h after the injection, were anaesthetised with a mixture of ketamine and xylazine. D-luciferin (potassium salt; Biosynth, Staad, Switzerland) was injected into the peritoneal cavity of mice at 2 $mg \cdot kg^{-1}$. After 5 min, luciferase activity was detected from the ventral surface using a noninvasive bioimaging system (IVIS; Xenogen, Alameda, CA, USA) [13, 14].

Furthermore, to precisely quantify luciferase activity in individual organs, the liver (quadrate lobe), right lung, heart, kidney and spleen were excised from mice 24 h after the hydrodynamic gene transfer. 1 ml of Passive Lysis Buffer (Promega) was added to the organs and homogenised with a Polytron homogenizer (Kinematica, Littau, Switzerland).